

## A 7-DOF redundantly actuated parallel haptic device combining 6-DOF manipulation and 1-DOF grasping

Lambert, Patrice; Herder, Just L.

**DOI**

[10.1016/j.mechmachtheory.2019.01.002](https://doi.org/10.1016/j.mechmachtheory.2019.01.002)

**Publication date**

2019

**Published in**

Mechanism and Machine Theory

**Citation (APA)**

Lambert, P., & Herder, J. L. (2019). A 7-DOF redundantly actuated parallel haptic device combining 6-DOF manipulation and 1-DOF grasping. *Mechanism and Machine Theory*, 134, 349-364.  
<https://doi.org/10.1016/j.mechmachtheory.2019.01.002>

**Important note**

To cite this publication, please use the final published version (if applicable).  
Please check the document version above.

**Copyright**

Other than for strictly personal use, it is not permitted to download, forward or distribute the text or part of it, without the consent of the author(s) and/or copyright holder(s), unless the work is under an open content license such as Creative Commons.

**Takedown policy**

Please contact us and provide details if you believe this document breaches copyrights.  
We will remove access to the work immediately and investigate your claim.



## Research paper

# A 7-DOF redundantly actuated parallel haptic device combining 6-DOF manipulation and 1-DOF grasping<sup>☆</sup>

Patrice Lambert<sup>\*</sup>, Just L. Herder

Department of Precision and Microsystems Engineering, Delft University Technology, Delft, the Netherlands



## ARTICLE INFO

### Article history:

Received 10 October 2018

Revised 17 December 2018

Accepted 1 January 2019

Available online 10 January 2019

### Keywords:

Haptic devices

Haptic grasping

Redundant parallel robots

Configurable platform

Kinematics

## ABSTRACT

Parallel manipulators are often used in haptic applications since they usually offer higher stiffness and lower inertia than their serial counterparts. However, classical parallel haptic devices generally do not provide grasping capabilities since all their motors are located at the base. This article presents a new 7-DOF robotic architecture, which has the particularity of providing 1-DOF grasping in addition to 6-DOF manipulation while all actuators are located at the base. This is possible thanks to the use of a novel configurable platform that replaces the single rigid body normally used as end-effector in conventional parallel manipulators. The grasping capability of this haptic device is part of the mechanical architecture itself and can be fully controlled from base-located motors. In this article, the architecture, kinematic analysis, kinematic performance, design, and implementation of the novel 7-DOF parallel haptic device are described.

© 2019 Elsevier Ltd. All rights reserved.

## 1. Introduction

To provide realistic force feedback, impedance controlled haptic devices need to be lightweight, such that the inertia of the devices themselves do not disturb the rendered forces, and they need to be stiff, such that the devices can mechanically present high frequency content forces. Lightness and stiffness are two naturally opposed qualities in mechanics, and the ratio of stiffness over weight has sometimes been termed structural stiffness. In order to maximize their structural stiffness, most haptic devices are nowadays based on a parallel robotic structure [1–7]. Parallel robotic devices are characterized by multiple kinematic connections, i.e. legs, between their end-effector and the base, which allows all motors to be mounted on the base. They usually offer high stiffness and low inertia in comparison with their serial counterparts [8,9].

Although parallel robotic architectures offer higher structural stiffness which allows better mechanical interactions, their main drawbacks are that they can present parallel singularities within the workspace [10], are generally limited in rotational motion and do not provide grasping capabilities. It can however be desirable to provide grasping force feedback via multiple contact points to allow the operator to feel the shape and stiffness of the manipulated objects, as he/she would do naturally with bare hands or with a grasping tool. This would allow the operator to interact with the remote or virtual environment in a more natural way than through a single contact point.

The common solution to provide haptic grasping is to mount an actuated grasper on an existing haptic device. Additional mounted motors are also sometimes used to provide rotational DOF to the interface [11]. However, the main advantage of

<sup>☆</sup> Research supported by the Dutch Technology Foundation STW.

<sup>\*</sup> Corresponding author.

E-mail address: [patrice.lambert@kcl.ac.uk](mailto:patrice.lambert@kcl.ac.uk) (P. Lambert).

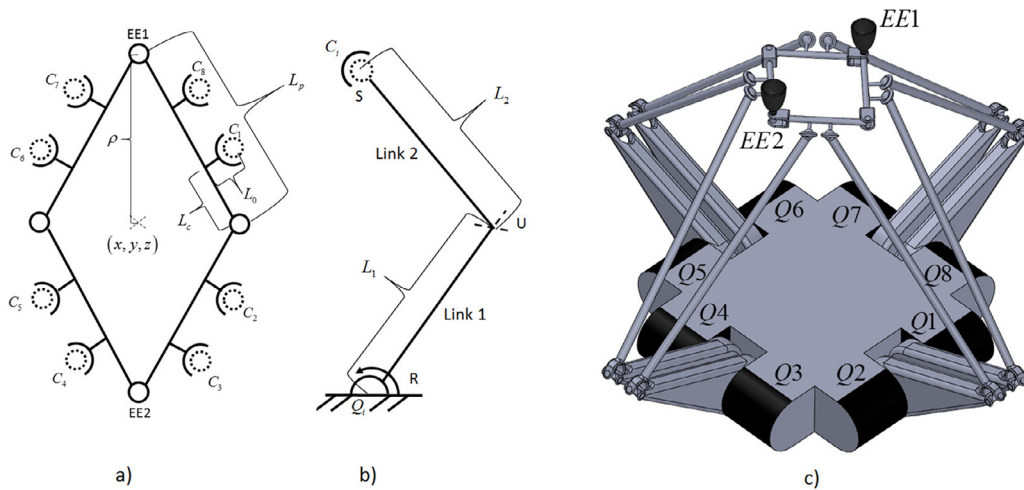


**Fig. 1.** a) Schema and notation of the 1-DOF planar configurable platform, with 2 fingertip interfaces located at EE1 and EE2. b) The 8 identical legs, formed by an actuated revolute joint (R) located on the base, a passive universal joint (U) and a passive spherical joint (S). c) Simplified CAD representation of the complete haptic device. The position/orientation or force/torque of the two fingertip interfaces EE1 and EE2 is fully controlled by the 8 actuators  $Q_i$ , located on the base.

parallel robots -the fact that all the motors are located on the base- is lost when this approach is implemented. Bowden cable transmissions could also be used to provide grasping from base-located motors [12], but they can produce Coulomb friction, viscous friction, stiction, and stick-slip at the end-effector, which is especially unwanted in an impedance controlled haptic device. They also require maintenance as they can wear more easily than rigid links and bearings.

The novel robotic architecture presented in this paper offers 7-DOF, combining 1-DOF haptic grasping and 6-DOF manipulation, while all the motors are located at the base. This is accomplished without the use of any electric wires or Bowden cables to actuate and sense the grasping position. Instead, the gripper is part of the mechanical architecture itself and the only components between the actuated joints on the base and the grasper are mechanical links and passive joints.

This is possible thanks to a novel configurable platform. In this novel type of robotic architecture, the rigid platform at which the haptic grasper would be normally connected is replaced by a closed-loop mechanical chain, a configurable platform [13–15], presenting 1 internal DOF. Both the pose (position and orientation) and the configuration of the grasper is fully controlled from the motors located on the base. The total number of DOF of the device is therefore 7. A redundantly actuated concept involving 8 identical parallel legs with base-located actuators is used to control the 7-DOF of the haptic interface. Actuation redundancy improves the quality of the transfer function between the motors and the haptic grasper and allows for a symmetrical design which improves the homogeneity of the performance and simplifies its analysis and implementation.

This article is an extension of the work introduced in [16], and includes a more detailed description as well as extensive additional simulation results. Those results show that configurable platforms can be used to include grasping capabilities in a haptic device and that a kinematic solution for the design parameters of this architecture can be found that satisfies the basic human ergonomic requirements (workspace, resolution, force capabilities), using commonly available motors and sensors.

Section 2 of this article introduces and describes the novel robotic architecture, Section 3 presents its kinematic analysis, Section 4 describes the selection of the kinematic design, Section 5 presents its resulting kinematic properties over the 7-DOF workspace, and Section 6 shows the implementation of the proposed solution into a functional prototype.

## 2. Architecture description

This section describes the mechanical architecture on which the 7-DOF haptic device is based. The main difference with classical parallel haptic devices is the presence of a 1-DOF configurable platform that replaces the rigid end-effector platform. This additional DOF is used to provide grasping capabilities via two interaction points located on the platform that can be connected to the human fingertips.

### 2.1. Configurable grasping platform

The 1-DOF grasping platform is formed by four identical rigid links of length  $L_p$ , assembled in closed-loop as a planar rhombus by four revolute joints, as shown in Fig. 1a. Two of the revolute joints are used to position the two thimble-shaped fingertip interfaces (the two end-effectors), which are labelled as EE1 and EE2. Each rigid link has two legs attached to points  $C_i$ , where spherical joints connect the 8 parallel legs to the platform. The positions of the spherical joints on the platform

links are defined by  $L_c$ , the distance to the nearest platform joint, and  $L_o$ , the offset from the link centre line. The offset distance  $L_o$  was necessary for the technical implementation of the prototype. The values of  $L_c$  and  $L_o$  are respectively the same for all leg attachment points. The configuration of the platform is defined by the grasping value  $\rho$ , the half distance between the fingertips. The position of the platform is defined by the coordinates  $(x, y, z)$  of a virtual point located at the midpoint of a line between the two end-effectors axis, and in the same plane as the platform and the spherical joints. The two diagonals of the rhombus linkage can be associated with a  $x$  and  $y$  axes to define the relative orientation of the platform with the base, using 3 Euler angles  $(\alpha, \beta, \gamma)$ .

### 2.2. Parallel legs

The pose (position/orientation), and the grasping configuration of the platform are controlled by 8 identical parallel legs, each having one actuated joint located on the base. The device is redundantly actuated since the 7-DOF of the architecture are controlled by 8 independent actuators. Actuator redundancy was chosen in order to allow a symmetrical design. It is also commonly accepted that parallel robots with actuation redundancy are less prone to have parallel singularities within their workspace [17–19] since the Jacobian matrix rank deficiency condition for parallel singularity in redundant devices applies on a rectangular matrix rather than the square one found in non-redundant parallel devices. Each leg has two rigid links of length  $L_1$  and  $L_2$  and has an actuated 1-DOF revolute joint (R) located at the base, a 2-DOF universal joint (U) between the two rigid links, and a 3-DOF spherical joint (S) connecting the leg to the configurable platform, as shown in Fig. 1b. Each leg possesses therefore 6-DOF in total and does not apply any constraints on the platform when the base actuated joint is free. The position and orientation of the actuators were chosen such that two actuators connecting to the same platform link always have their orientations perpendicular to each other and that the leg segments connecting to the platform also form an angle close to  $90^\circ$  in the centre configuration. Fig. 1 shows a representation of the configurable platform, the legs, and the complete haptic device.

### 3. Kinematic analysis

This section introduces the kinematic analysis of the 7-DOF parallel haptic device and describes the mathematical relations for the position, velocity and static force transmission between the 7 dimensions of the end-effectors space and the 8 dimensions of the actuators space. Due to the presence of the configurable platform, the kinematic analysis of this 7-DOF haptic device must be solved in two distinct steps, as described in [15]. Before presenting the kinematic analysis, let's define position vectors and force vectors for both the 8 coordinates of the actuators space and the 7 coordinates of the end-effectors space. We have

$$\begin{aligned} \chi &= [x \quad y \quad z \quad \alpha \quad \beta \quad \gamma \quad \rho]^T & \mathbf{q} &= [q_1 \quad q_2 \quad q_3 \quad q_4 \quad q_5 \quad q_6 \quad q_7 \quad q_8]^T \\ \mathbf{f} &= [f_x \quad f_y \quad f_z \quad \tau_\alpha \quad \tau_\beta \quad \tau_\gamma \quad f_\rho]^T & \boldsymbol{\tau} &= [\tau_1 \quad \tau_2 \quad \tau_3 \quad \tau_4 \quad \tau_5 \quad \tau_6 \quad \tau_7 \quad \tau_8]^T \end{aligned} \quad (1)$$

$\chi$  is the position vector of the end-effector, in which  $x, y$  and  $z$  correspond to the position of the middle point of the configurable platform,  $\alpha, \beta$ , and  $\gamma$  represent successive Euler rotations around the Z axis, Y axis, and X axis of the platform reference frame respectively,  $\rho$  represents the half distance between the two gripper tips.

$\mathbf{q}$  is the position vector of the 8 actuators, where  $q_i$  represents the angular position of link 1 of leg  $i$ , relatively to the horizontal plane. Vectors  $\mathbf{f}$  and  $\boldsymbol{\tau}$  are the force vector counterparts to the position vector  $\chi$  and  $\mathbf{q}$  respectively, where  $f_i$  represents linear force along element  $i$  and  $\tau_i$  represents torque around element  $i$ .

#### 3.1. Inverse position kinematics

The inverse position kinematics establishes the position of the actuators as a function of the end-effector positions. We are looking to define the system of 8 non-linear functions  $\mathbf{q} = H_{IPK}(\chi)$ .

The first end-effector coordinate to consider is the grasping value  $\rho$ , which defines the platform configuration. Fig. 1a shows the position of the 8 leg attachment points  $C_i$ , for a certain grasping value  $\rho$ . The vector  $\mathbf{c}_{pi}$ , that goes from the middle point of the platform  $(x, y, z)$  to the attachment point of leg  $i, C_i$ , can be calculated in the platform reference frame as:

$$\begin{aligned} \mathbf{c}_{p1} &= [a_2 \quad b_1 \quad 0]^T & \mathbf{c}_{p2} &= [a_2 \quad -b_1 \quad 0]^T & \mathbf{c}_{p3} &= [a_1 \quad -b_2 \quad 0]^T & \mathbf{c}_{p4} &= [-a_1 \quad -b_2 \quad 0]^T \\ \mathbf{c}_{p5} &= [-a_2 \quad -b_1 \quad 0]^T & \mathbf{c}_{p6} &= [-a_2 \quad b_1 \quad 0]^T & \mathbf{c}_{p7} &= [-a_1 \quad b_2 \quad 0]^T & \mathbf{c}_{p8} &= [a_1 \quad b_2 \quad 0]^T \end{aligned} \quad (2)$$

where

$$a_1 = \frac{L_c \sqrt{L_p^2 - \rho^2} + L_o \rho}{L_p} \quad a_2 = \frac{(L_p - L_c) \sqrt{L_p^2 - \rho^2} + L_o \rho}{L_p} \quad b_1 = \frac{L_c \rho + L_o \sqrt{L_p^2 - \rho^2}}{L_p} \quad b_2 = \frac{(L_p - L_c) \rho + L_o \sqrt{L_p^2 - \rho^2}}{L_p} \quad (3)$$

Once the position of each leg attachment point  $\mathbf{c}_{pi}$  is defined as a function of the platform configuration  $\rho$  in the platform reference frame, the leg attachment point  $\mathbf{c}_{oi}$  can be expressed in the global reference using

$$\mathbf{c}_{oi} = [x \quad y \quad z]^T + \mathbf{R}(\alpha, \beta, \gamma) \mathbf{c}_{pi} \quad (4)$$

where  $\mathbf{R}(\alpha, \beta, \gamma)$  is the  $3 \times 3$  rotation matrix representing the orientation of the platform after successive rotations around the  $x$ ,  $y$ , and  $z$  axis in the global reference frame such that  $\mathbf{R} = \mathbf{R}_z(\alpha)\mathbf{R}_y(\beta)\mathbf{R}_x(\gamma)$  and  $[x \ y \ z]^T$  is the position of the middle of the platform. Once the 8 leg attachment points  $C_i$  are known, it is possible to calculate the angular value of the 8 actuators. Since all legs have the same architecture, all 8 actuator positions can be calculated using the same procedure.

For each leg attachment point  $C_i$ , we can define the vector  $\mathbf{c}_{li}$ , which correspond to the position vector  $\mathbf{c}_{0i}$ , but expressed in a coordinate frame located at the actuator position of leg  $i$  and oriented such that its  $Z$  axis corresponds to the axis of rotation of the actuator and its  $X$  axis and  $Y$  axis correspond to the horizontal plane and vertical plane respectively. The closure equation for leg  $i$  can then be expressed as

$$|\mathbf{c}_{li} - [L_1 \cos(q_i) \quad L_1 \sin(q_i) \quad 0]|^2 = L_2^2 \tag{5}$$

where  $q_i$  is the angular value of the actuator. Developing Eq. (5) leads to

$$c_{lix} \cos(q_i) + c_{liy} \sin(q_i) = \frac{|\mathbf{c}_{li}|^2 + L_1^2 - L_2^2}{2L_1}. \tag{6}$$

Finally, using the tangent half-angle substitution in Eq. (6), the actuator angle  $q_i$  is obtained as

$$q_i = 2 \tan^{-1} \left( \frac{c_{liy} + \sqrt{c_{liy}^2 + c_{lix}^2 - w^2}}{w + c_{lix}} \right) \tag{7}$$

where  $w = (|\mathbf{c}_{li}|^2 + L_1^2 - L_2^2) / 2L_1$ .

### 3.2. Inverse velocity kinematics

The inverse velocity kinematics describes the local linear mapping from the 7 coordinates of the end-effector velocity to the 8 actuators velocities. The linear relation is given in the form of a rectangular Jacobian matrix  $\mathbf{J}$ :

$$\dot{\mathbf{q}}_{(8 \times 1)} = \mathbf{J}_{(8 \times 7)} \dot{\boldsymbol{\chi}}_{(7 \times 1)}. \tag{8}$$

The linear relation is only valid locally, so the elements in  $\mathbf{J}$  must be updated as the device changes its configuration. Due to the presence of the configurable platform, the inverse velocity kinematics of this device must also be solved in two steps. One step consists in the calculation of the platform Jacobian matrices  $\mathbf{J}_{pi}$ , which relate the end-effector velocity  $\dot{\boldsymbol{\chi}}$  to the leg attachment point velocity  $\dot{\mathbf{c}}_{0i}$  of leg  $i$ . The second step consists in the calculation of the leg Jacobian matrices  $\mathbf{J}_{li}$  which represents the mapping between the leg attachment point velocity  $\dot{\mathbf{c}}_{0i}$  and the actuator angular velocity  $\dot{q}_i$ . Once the expressions for all  $\mathbf{J}_{pi}$  and  $\mathbf{J}_{li}$  are found, the total Jacobian  $\mathbf{J}$  can be assembled as

$$\mathbf{J}_{(8 \times 7)} = \begin{bmatrix} \mathbf{J}_{l1,(1 \times 3)} \mathbf{J}_{p1,(3 \times 7)} \\ \vdots \\ \mathbf{J}_{li,(1 \times 3)} \mathbf{J}_{pi,(3 \times 7)} \\ \vdots \\ \mathbf{J}_{l8,(1 \times 3)} \mathbf{J}_{p8,(3 \times 7)} \end{bmatrix}. \tag{9}$$

First, each platform Jacobian matrix  $\mathbf{J}_{pi}$  can be expressed in the form

$$\mathbf{J}_{pi,(3 \times 7)} = [\mathbf{I}_{(3 \times 3)} \quad \boldsymbol{\Omega}_{i,(3 \times 3)} \quad \mathbf{G}_{i,(3 \times 1)}] \tag{10}$$

where  $\boldsymbol{\Omega}_{i,(3 \times 3)}$  is the matrix of angular velocity and  $\mathbf{G}_{i,(3 \times 1)}$  represents the velocity of attachment point  $C_i$  as a function of the grasping velocity  $\dot{\rho}$ , such that  $\dot{\mathbf{c}}_{0i} = \mathbf{J}_{pi} \dot{\boldsymbol{\chi}}$ . The matrix  $\boldsymbol{\Omega}_i$  and vector  $\mathbf{G}_i$  are dependent on the angular position of the platform and its grasping configuration respectively.

Fig. 2 provides a geometrical interpretation of the relation between the instant grasping velocity  $\dot{\rho}$  and the instant velocity of the leg attachment points  $\dot{\mathbf{c}}_{0i}$ . As the platform changes its configuration due to grasping velocity, each platform link instantaneously rotates around a point located at the corners of the dotted rectangle. The  $\mathbf{r}_i$  vectors can be calculated directly from the inverse position kinematics.  $\hat{\mathbf{r}}_p$  is a unit vector perpendicular to the plane of the platform and to all  $\mathbf{r}_i$ . Some of the vectors  $\mathbf{r}_i$  are directed to the platform and some are directed from the platform depending on the direction of rotation of the platform links as a function of a positive grasping velocity. The 8 vectors  $\mathbf{G}_i$  relating grasping velocity to the leg attachment point velocity are given by

$$\mathbf{G}_{i,(3 \times 1)} = \frac{\hat{\mathbf{r}}_p \times \mathbf{r}_i}{\sqrt{L_p^2 - \rho^2}}. \tag{11}$$

The numerator in the previous equation represents the linear velocity due to a unit angular velocity around the corners of the dotted rectangle and the denominator correlates the rotation velocity to the grasping velocity  $\dot{\rho}$ .

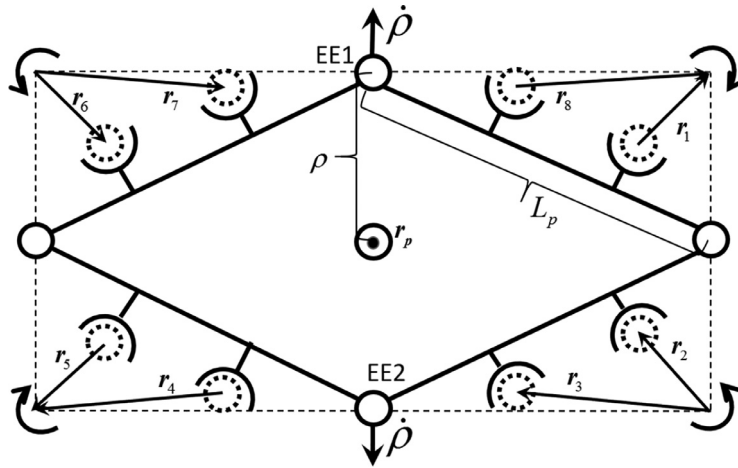


**Fig. 2.** Relation between instant grasping velocity  $\dot{\rho}$  and instant leg attachment point velocity  $\dot{c}_i$ : The leg attachment points will rotate around the corners of the dotted rectangle as the platform changes configuration.

The angular velocity matrix  $\Omega_i$  relates the angular velocity vector  $[\dot{\alpha} \ \dot{\beta} \ \dot{\gamma}]^T$  -which corresponds to angular velocity around the Z axis, Y axis, and X axis- to the leg attachment point velocity  $\dot{c}_i$ .  $\Omega_i$  is given by

$$\Omega_i = \begin{bmatrix} -c_{0iy} & c_{0iz}C_\alpha & c_{0iz}S_\alpha C_\beta + c_{0iy}S_\beta \\ c_{0ix} & c_{0iz}S_\alpha & -c_{0iz}C_\alpha C_\beta - c_{0ix}S_\beta \\ 0 & -c_{0iy}S_\alpha - c_{0ix}C_\alpha & c_{0iy}C_\alpha C_\beta - c_{0ix}S_\alpha C_\beta \end{bmatrix} \tag{12}$$

where  $C_\alpha, C_\beta, S_\alpha$  and  $S_\beta$  are the cosines and sines of angle  $\alpha$  and  $\beta$ .

The leg Jacobian matrices  $J_{li}$  represent the mapping between the leg attachment point velocities  $\dot{c}_i$  and the actuator angular speeds  $\dot{q}_i$ . Since all legs are identical, their Jacobian matrices can be described using the same formula:

$$J_{li,(1 \times 3)} = \frac{\hat{l}_{i2}^T}{(\hat{s}_i \times l_{i1}) \cdot \hat{l}_{i2}} \tag{13}$$

where  $l_{i1}$  is a vector along link 1 and of the same length,  $\hat{l}_{i2}$  is a unit vector along link 2, and  $\hat{s}_i$  is a unit vector along the axis of rotation of the leg actuator.

The total Jacobian  $J_{(8 \times 7)}$  can finally be assembled as in Eq. (9). The resulting Jacobian matrix will be useful in the next sections for the computation of the forward position kinematic, static force transmission, and kinematic performance analysis.

### 3.3. Forward position kinematics and statics

Since the human operator interacts with the haptic device and influences its position, a forward position kinematics (FPK) model is needed to determine the positions of the end-effectors EE1 and EE2 as a function of the actuator sensor positions. We are looking for a solution to the system of 7 non-linear equations  $\chi = H_{FPK}(\mathbf{q})$ .

As usual for parallel robotic devices, the forward kinematic problem is very difficult or impossible to solve analytically. Given the 8 actuator positions  $\mathbf{q}$ , we can determine the position of the middle universal joint U for each leg. In order to find a solution to  $H_{FPK}$ , one must now determine for which combination of position, orientation and grasping configuration, every leg attachment point  $C_i$  of the platform can lie on the surface of 8 spheres of radius  $L_2$ , centred on the middle of joint U of each leg. This problem involves highly coupled non-linear equations, which have usually multiple solutions, and for which no closed-form solutions are available. Instead of an analytical solution, we implemented a numerical procedure using the Jacobian matrix  $J$  found in the previous section. For small displacements, we can use the relation

$$\Delta \chi = J_{(7 \times 8)}^+ \Delta \mathbf{q} \tag{14}$$

where the rectangular direct Jacobian  $J^+ = (J^T J)^{-1} J^T$  is obtained numerically from the Moore-Penrose pseudoinverse of the rectangular inverse Jacobian matrix found in (9). Given an initial estimate of the end-effector position  $\chi_{est}$ , we can use the following numerical procedure to solve  $H_{FPK}$ :

$$\begin{aligned} \mathbf{q}_{est} &= H_{IPK}(\chi_{est}) \\ \Delta \mathbf{q} &= \mathbf{q}_{est} - \mathbf{q}_{sensors} \\ \Delta \chi &= J^+ \Delta \mathbf{q} \\ \chi_{est,2} &= \chi_{est} + \Delta \chi \end{aligned} \tag{15}$$

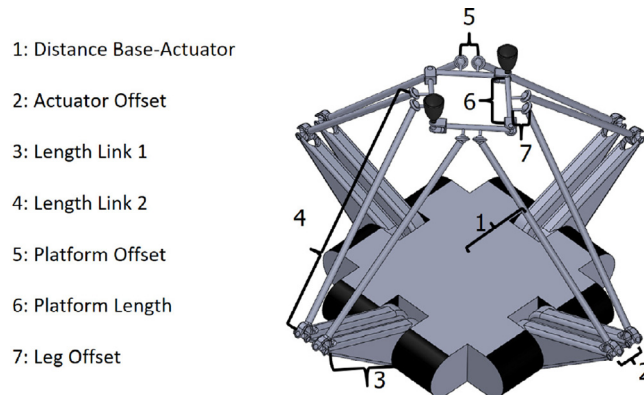


Fig. 3. The 7 kinematic design parameters.

where  $\chi_{est}$  is replaced by the new estimate  $\chi_{est, 2}$  after each iteration. In theory, the convergence criteria  $\Delta \mathbf{q}_{min}$ , stopping the procedure, should be equal to the resolution of the sensors. In practice, small errors in the calibration mean that the part of  $\Delta \mathbf{q}$  that can be projected into the null space of  $\mathbf{J}^+$  do not contribute to the position correction  $\Delta \chi$ . For this reason, the FPK procedure is stopped when the norm of  $\Delta \mathbf{q}$  does not decrease by the sensor resolution after a certain number of iterations. The residual error in the final  $\Delta \mathbf{q}$  is then aligned with the null space of  $\mathbf{J}^+$  and is due to calibration.

This procedure is mathematically equivalent to a Gauss–Newton algorithm used to solve non-linear least squares problems and is repeated at each sample time in the control system. In order to converge to a particular solution that minimizes  $\Delta \mathbf{q}$ , the initial guess should be close enough to the actual solution and the Jacobian matrix should not be ill-conditioned. Those are reasonable assumptions since the initial guess used at each sampling time is the solution found in the previous sampling time, and that no singularities were detected inside the  $\hat{a}g_{useful} workspace \hat{a}g$  (defined in Section 5.1). A mechanical stopper on each leg was used to provide an accurate first guess when starting the real-time control system.

Now that the position of the end-effectors EE1 and EE2 can be determined as a function of the 8 sensors angles, located on the base, we need to determine the force mapping from the motors located on the base to the operator's hand, in order to provide the proper force feedback in this position. Using the power conservation principle, the static mapping between  $\mathbf{f}$  and  $\boldsymbol{\tau}$  is calculated by

$$\boldsymbol{\tau} = (\mathbf{J}^+)^T \mathbf{F}. \quad (16)$$

Since the device has actuator redundancy, the desired end-effector force  $\mathbf{f}$  can in principle be produced by an infinite number of solutions for  $\boldsymbol{\tau}$ . However, using the Moore–Penrose pseudoinverse provides the solution with the minimum norm of the vector  $\boldsymbol{\tau}$ .

#### 4. Kinematic design

Once the kinematic relations of the device have been defined as a function of its design parameters, a kinematic design can be selected. The kinematic design includes all design parameters having an influence on the kinematic performance. The requirements on those performances, including the workspace, the resolution and the force mapping between the device grasper tips and the actuator/sensors are driven by human ergonomics. Resolution and force mapping also vary for each configuration  $\chi$  within the 7-DOF workspace of the robot. Other design parameters, such as the cross section of the links, the material chosen etc. may have an effect on the mechanical bandwidth of the device but do not influence its kinematic performance. In Sections 4 and in 5, only the kinematic design is considered and the remaining design parameters will be discussed in Section 6.

##### 4.1. Design parameters

The highly symmetrical architecture of the device allows us to considerably reduce the number of design parameters. Assuming identical lengths for the 4 links of the configurable platform, identical legs, and identical distances between the motors and the centre of the base, the robot can be fully defined using only 7 parameters. These parameters are shown in Fig. 3.

Furthermore, it was realised in the early stages of the design that the kinematic performance, which can be investigated by calculating the condition number of the Jacobian matrix using the GUI tool that will be described in Section 4.2, was better in average over the workspace when the offset kinematic parameters 2, 5 and 7 were set to a minimum, regardless of the remaining parameters. These parameters were therefore constrained by the technical implementation of the prototype, which will be presented in Section 6. Parameter 6, which defines the dimensions of the configurable platform must be set

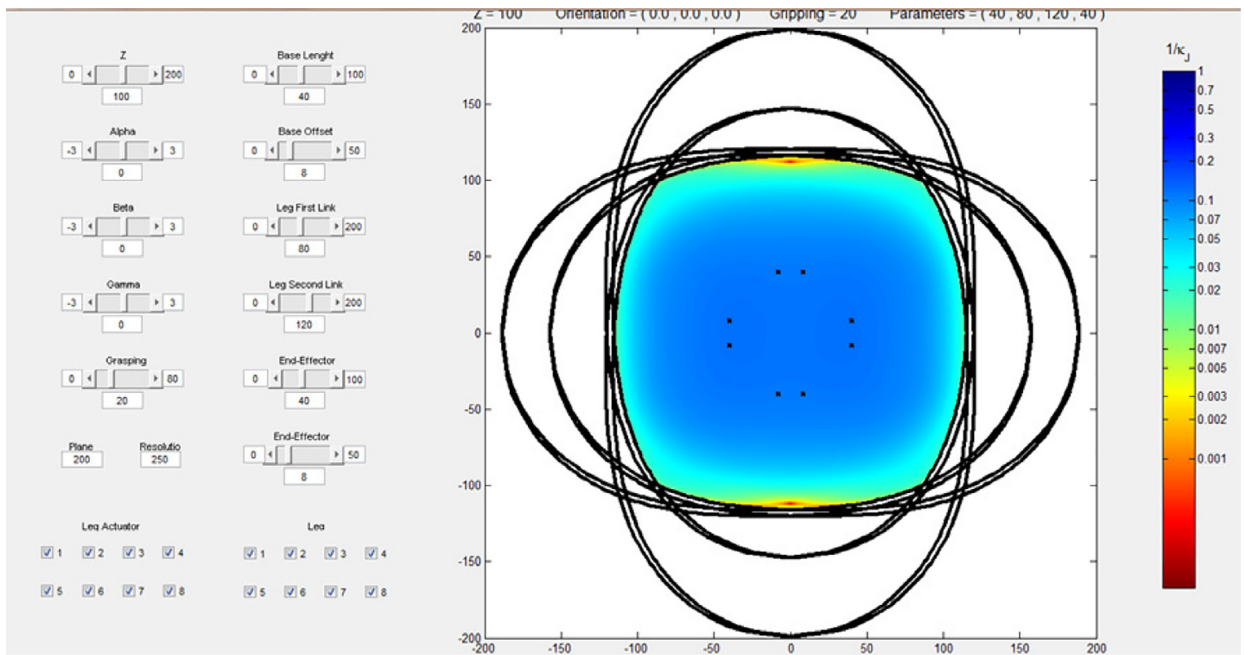


Fig. 4. A GUI application developed to analyse the performance of the 7-DOF haptic device. A dense sampling in the XY plane can be performed while sliders allow variations of the remaining dimensions of the workspace as well as the kinematics design parameters.

such that the distance between the two fingertips during grasping respects the ergonomics of human grasping. There is a limit on the lowest grasping value since the configurable platform cannot completely fold on itself without mechanical interference. The interval of grasping distance between the fingertips, i.e. twice the grasping value  $\rho$ , was therefore set to [40, 90] mm. This left the number of kinematics parameters to select to only three; the distance between the centre of the base and the actuators, and the length of link 1 and link 2 of the legs.

#### 4.2. Design evaluation

Since the device is highly symmetrical, one can expect the same type of symmetry in the performance throughout the workspace. Several kinematic properties of the device for a certain configuration can be extracted numerically from the properties of the Jacobian matrix, such as the resolution and force mapping between the end-effectors and the actuator as well as the workspace boundaries and the presence of singularities. The complexity in evaluating the overall kinematic performance comes from the high number of DOF of the device and the fact that all the DOF are kinematically coupled. The Jacobian matrix is dependent on the position/orientation/grasping of the device in its 7-DOF over the workspace and the total number of sampling points grows to the power 7 with the number of sampling points in each dimension. In addition, each point evaluated has a different resolution and force capability in each direction of the 7-DOF.

As a first step, it was therefore chosen to perform a dense sampling ( $<1$  mm) on the 2D horizontal plane (X, Y) subspace for various sets of values for the remaining dimensions and investigate the kinematics properties based on the Jacobian matrix for those subspaces. A graphical user interface (GUI) tool was developed in Matlab to represent several kinematics properties of the robot in the XY plane of the workspace and for constant values of the other workspace dimensions. Sliders on the GUI can be used to change the remaining workspace dimensions as well as the kinematic design parameters. Fig. 4 shows a contour plot of the inverse of the condition number of the Jacobian matrix in the GUI environment developed. The workspace of each individual leg and the position of the actuators are also shown.

Among other performance indices, such as resolution and force capabilities, the condition number of the Jacobian matrix was investigated in order to detect the presence of possible singular configurations. The condition number here is defined as the ratio of the highest to lowest singular value of the Jacobian  $\mathbf{J}$ . If one of the singular value becomes null, the corresponding singular vector will represent a particular end-effector velocity  $\dot{\mathbf{x}}$  that produces no actuator motion  $\dot{\mathbf{q}} = \mathbf{0}$ , resulting in a parallel singularity. A characteristic length of 36mm, corresponding to the grasping average value, was used to convert angle units (rad) into length units (mm) in order to compare the different units while computing the condition number. Using this particular conversion ratio does not influence the configurations under which the condition number would become infinite, but gives a better representation of the dexterity of the device.

For each set of design parameters that were investigated with the GUI, the performance indices were analysed for various height (Z) of the XY plane for all combinations of the 3 orientations for values of  $30^\circ$ ,  $45^\circ$ , and  $60^\circ$  and grasping values  $\rho$



**Table 1**  
Kinematic design parameters.

#	Parameter	Value
1	Distance base-actuator	110 mm
2	Actuator Offset	30 mm
3	Length of Link 1	100 mm
4	Length of Link 2	297 mm
5	Platform Offset	15 mm
6	Platform length	51 mm
7	Leg Offset	14.5 mm

for 20, 36, and 47 mm. Using this information, the 3 kinematic design parameters that were still not fixed (1,3, and 4; corresponding to the length of the legs and their distance to the centre of the base) were investigated to improve the size of the workspace, the resolution, and the force mapping.

No parallel singularities were detected within the final “useful workspace” (defined in Section 5.1). Serial singularities are present at the boundaries of the workspace when those boundaries are the results of the robot dimensions and not created by the actuator angle limits. A formal proof for the position of singularities would imply finding the mathematical conditions for which the Jacobian matrix  $\mathbf{J}$  lost full rank. Since each element of the matrix is already a complicated analytical expression, and that the matrix is of dimension  $8 \times 7$ , the derivation of an analytical condition for parallel singularities was not considered and is outside the scope of this article.

Kinematic parameters 1, 3 and 4 were finally selected to improve the compactness of the device, i.e. the ratio of the workspace (presented in Section 5.1) over the total length of the legs, while offering acceptable performance in terms of kinematics resolution and force mapping based on human ergonomics. This is discussed further in Section 5.

#### 4.3. Selected design

After the GUI tool was used as a preliminary investigation of the influence of the kinematic parameters on the performance of the robot, the most promising sets of design parameters can then be evaluated formally with a sampling that is less dense but that cover the whole 7-DOF workspace to assess their performance, as it will be presented in Section 5.

The selected kinematic design parameters are shown in Table 1. Offsets between joints were chosen as low as technically possible. The platform dimension was defined by ergonomics of the operator and the distance of the motors to the base and the length of the leg links were chosen based on an evaluation of forces and resolution mapping over the whole workspace. The resulting workspace, resolution and force mapping are presented in the next section.

### 5. Kinematic specifications of the selected design

This section presents some of the resulting kinematic properties of the selected design, such as the forces and resolution mappings between the grasper tips and the actuator/sensors at the base over the 7-DOF workspace of the device.

#### 5.1. Workspace

A graphical representation of the workspace of the 7-DOF haptic device is complicated by the fact that the workspace boundaries are coupled in all 7 dimensions. Given the size of the configurable platform relatively to the length of the parallel legs, the translational workspace is mainly limited by the workspace of each individual leg. The workspace of an individual leg is determined by its length when fully extended, but also by the ranges on the joints angles. Actuator angular values in  $\mathbf{q}$  are limited between  $-55^\circ$  and  $+90^\circ$  due to their technical design. The orientation workspace is also sometimes limited by physical interference between the legs, or between the legs and the platform, for large orientations in the centre of the workspace. The grasping workspace is generally limited by collisions between the links of the platform, except for position at the border of the translational and/or orientation workspaces.

The translational workspace corresponds here to all possible locations that can be reached by the centre point of the configurable platform with a given orientation and a given grasping value. In this design, it occurs that the dimensions of the horizontal workspace in the XY plane always get smaller for higher vertical values on the Z axis. This allows us to represent the 3D translational workspace in a topographic 2D graph where the plane represents the X and Y axis and the isolines represent the Z axis.

Fig. 5 shows the translational workspaces for six sets of constant orientations and constant grasping. The first graph corresponds to the translational workspace when all other dimensions are at their central values, the next four graphs corresponds to a single off-centre orientation or grasping value, and the last one corresponds to a mixture of off-centre orientations and grasping. The lowest isoline corresponds to the lowest horizontal slide of the workspace that did not have had any void in it.

Table 2 summarizes the limits of each dimension of the workspace when the other dimensions are in their centre position ( $x = y = 0$  mm,  $z = 270$  mm,  $\alpha = \beta = \gamma = 0$ ,  $\rho = 36$  mm). In reality, the boundaries for the different DOF of the

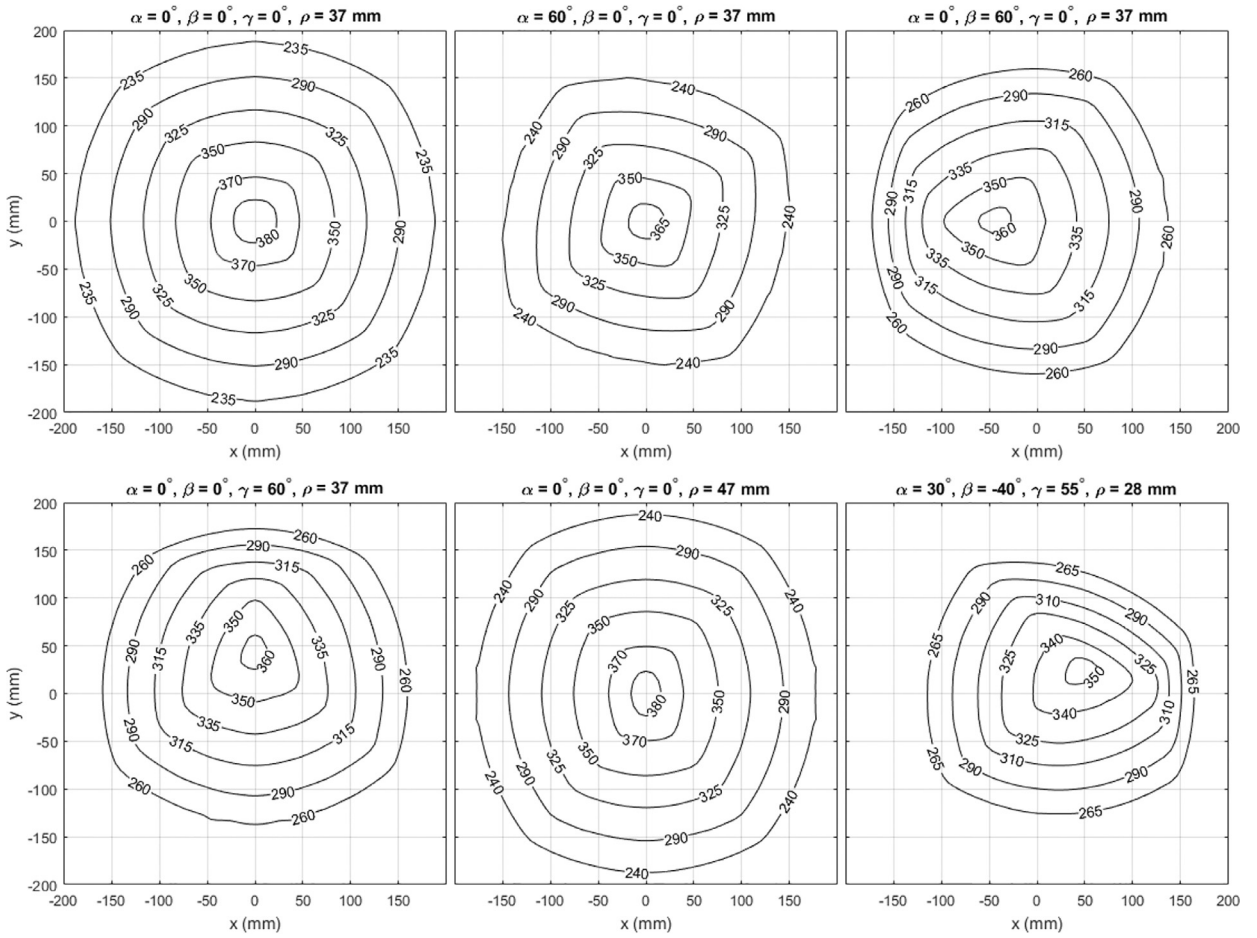


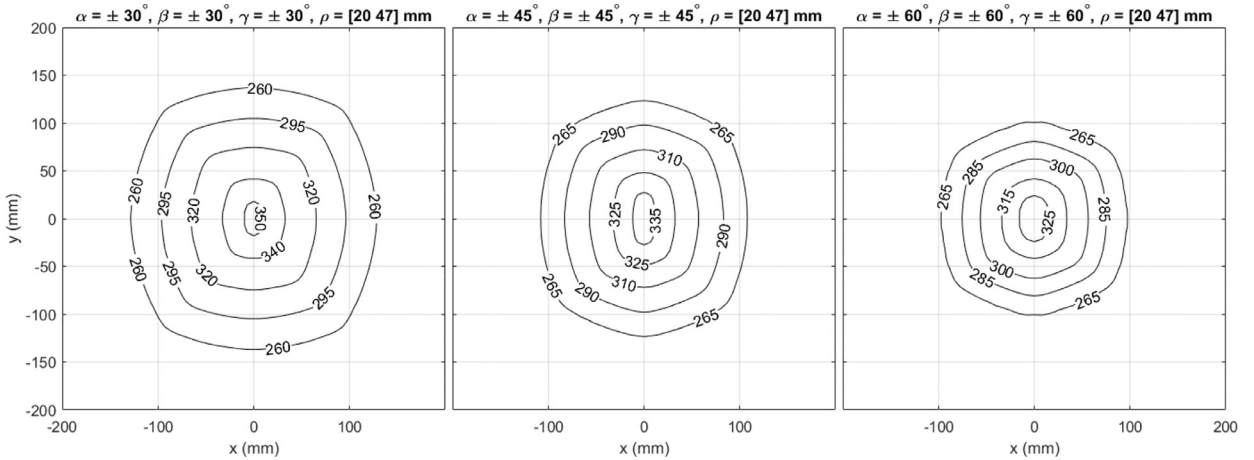
Fig. 5. Height (mm) of the translational workspace for six sets of constant orientations and constant grasping.

Table 2  
Workspace central boundaries.

Dimension	Value
X Axis	± 166 mm
Y Axis	± 166 mm
Z Axis	184 mm–386 mm
Rotation around X axis	± 74°
Rotation around Y axis	± 74°
Rotation around Z axis	± 80°
Grasping	40 mm–94 mm

workspace are all coupled, as shown in Fig. 5, and the limits of the workspace are reduced when the other dimensions of the configuration are not centred.

When manipulating the haptic device, the operator should not need to be aware of all the coupling between the workspace dimensions. For this purpose, we can determine a “useful workspace”, which can be defined as a region of the workspace where any orientation and any grasping are possible within certain intervals. The useful workspace is calculated using intersections of a sampling of translational workspaces over the 3 orientation intervals and the grasping interval. Fig. 6 shows the useful workspaces for orientation intervals of ±30°, ±45°, and ±60°. It can be seen that the translational dimensions of the useful workspace are reduced for larger orientation ranges. Despite the design being symmetrical in both X and Y axis, the useful workspace is slightly flattened in the y direction. This is only due to the Euler angle convention used to describe the 3 orientations. In fact, symmetrical useful workspaces would be obtained if the angular ranges were defined in term of tilting from a vertical axis, but since a Euler angles convention is used, successive equal orientation ranges results in a maximal tilting axis that is closer to the axis of the first rotation applied.



**Fig. 6.** Height (mm) of the translational useful workspace for a range of  $\pm 30^\circ$ ,  $\pm 45^\circ$ , and  $\pm 60^\circ$  Euler angular value ranges and a range of  $\rho = [20, 47]$  mm.

## 5.2. Resolution mapping

This section describes the kinematic relation between the sensors resolution and the grasper tips position and orientation resolutions over the workspace. The Jacobian matrix  $\mathbf{J}$  found in Eq. (9) can be used to describe locally the linear mapping between small displacements of the end-effectors  $\Delta\chi$  and small displacements of the actuators  $\Delta q$ . The method used here to calculate the device resolution is based on the sensitivity criteria presented in [20]. The advantage of this method is that position and orientation sensitivities, which have different units, can be represented independently as distinct criteria. The method is also well suited for redundantly actuated parallel devices since it does not require the pseudo-inverse computation of the Jacobian. We choose here to represent each dimension of the end-effector space separately.

Assuming that each sensor has a resolution of  $\Delta q_{\max}$ , the uncertainty in the actuator space can be defined as an 8-dimensional hypercube centred at the origin with an edge of size  $2 \times \Delta q_{\max}$ .

For each dimension  $j$  of the 7 dimensional end-effectors space, the problem of finding the worst error  $\Delta\chi_{j, \max}$ , due to maximal error in measurement  $\Delta q_{\max}$  in the 8-dimensional actuator space can be written as

$$\Delta\chi_{j, \max} = \max_{\chi} \hat{e}_j^T \chi$$

such that 
$$\begin{bmatrix} \mathbf{J} \\ -\mathbf{J} \end{bmatrix} \chi \leq \begin{bmatrix} \Delta q_{\max} \\ \vdots \\ \Delta q_{\max} \end{bmatrix}_{(16 \times 1)}$$
 (17)

where  $\hat{e}_j$  is a  $7 \times 1$  vector formed of null components except for the  $j^{\text{th}}$  which is 1, and  $\leq$  denotes the componentwise inequality. The inequality conditions represent the borders of the uncertainties in the actuator space and the fitness function represents the maximal possible value of the  $j^{\text{th}}$  element of the end-effector position vector  $\chi$ , regardless of the values of the other elements. Linear mapping of the hypercube from the actuator space into the end-effectors space results in a zonotope, i.e. a polytope for which each hypersurfaces has a corresponding hypersurface that is point-symmetrical through the origin point  $\mathbf{0}_8$ . Therefore a symmetrical limit on the error can be found as  $\Delta\chi_{j, \min} = -\Delta\chi_{j, \max}$ .

Formulating the problem in this way allows us to describe the sensitivity of each dimension of the workspace separately and allow us to solve the problem using Linear Programming, for which readily routines are available. The solution obtained represents the absolute boundaries of the  $j^{\text{th}}$  component of the total error due to the resolution of the sensors.

These solutions are of course dependent on the value of the Jacobian matrix for each configuration. In order to characterise the sensitivity of the device in each of the 7-DOF over the 7 dimensions of the workspace, the optimisation problem described in Eq. 17 has been solved for a large number of sampling points. Each of the 3 orientation dimensions  $\alpha$ ,  $\beta$ , and  $\gamma$  have been sampled for angular values of  $[-45^\circ, -22.5^\circ, 0^\circ, 22.5^\circ, 45^\circ]$ , grasping values have been sampled for [20, 28, 36, 42, 47] mm, and the translational dimensions  $x$ ,  $y$ , and  $z$  have been sampled with 1 cm intervals.

It was shown in Fig. 6 that, due to the coupled nature of the boundaries of the workspace, an infinity of useful workspaces can be considered depending on the desired angular ranges. In evaluating the kinematic design of this device, we choose to represent the resolution mapping for the useful workspace corresponding to a range of  $\pm 45^\circ$  for each rotation, shown in Fig. 6b, since it represents a reasonable compromise between translational and rotational ranges, and covers most of human wrist orientational capabilities. Using a sampling with all combination described in the previous paragraph, this resulted in 4,246,875 sampling points lying inside the useful workspace, for which the sensitivity has been calculated in each DOF. Linear Programming algorithm is relatively computer-intensive and the evaluation of the total set of

**Table 3**  
Resolution mapping for each DOF over the workspace.

DOF	Center	Mean	SD	Best	Worst
x (μm)	49.2	47.9	0.02	20.7	64.9
y (μm)	49.4	46.9	0.01	24.2	65
z (μm)	15.2	24.3	0.09	10.6	157
α (mrad)	0.868	1.35	5e-3	0.71	5.77
β (mrad)	0.648	0.816	8e-4	0.45	2.62
γ (mrad)	0.648	1.05	4e-4	0.539	2.65
ρ (μm)	32.3	35.9	0.03	14.8	88.2

sampling point requires a full day of computation on a regular desktop. Slightly less dense samplings were also performed with similar results, which suggests that increasing the sampling density would also not lead to significant different results.

Table 3 presents a summary of the resolution mapping from the actuators to the end-effectors over the workspace. The actuator resolution, defined by the sensor resolution and the transmission ratio used in the prototype implementation, is  $\Delta q_{max} = 0.131$  mrad. All relations being linear, using sensors with a different resolution would result in a corresponding linear change in the device sensitivity. Using these commonly available sensors, it can be seen that the average resolution in each dimension is well below a just-noticeable difference of 1mm for the human fingers static proprioception [21]. The low standard deviation (SD) shows that the kinematic resolution is near homogeneous over the useful workspace. It can also be noticed that these results are comparable to commercially available 7-DOF haptic devices, such as the Omega.7 from Force Dimension for example, which offer translational, rotation and grasping resolution of 100μm, 1.6 mrad, and 60μm respectively in its centre position.

### 5.3. Force mapping

In this section, the maximal forces and moments applicable to the grasper tips by the motors located on the base are presented over the whole 7-DOF workspace. The force mapping is given by Eq. (16), where the least-norm vector  $\tau$  in the 8-dimensional vector space of motor torques that can produce a desired force  $f$  is calculated as  $\tau = (J^+)^T f$ .

Although the governing equations of force mapping are similar to those describing the resolution mapping ( $\Delta q = J\Delta\chi$ ), the problem of finding the force capabilities of the device as a function of the actuator capabilities is quite different. Eq. 17 gives the maximal possible value of element  $j$  of  $\Delta\chi$  regardless of the value of the other elements. To determine the force capability in dimension  $j$ , we are interested in the maximal possible value of the element  $j$  of the vector  $f$  while all other elements are zero.

This problem is actually simpler to solve than the problem of the resolution mapping. We take here the approach presented in [22] to characterize locally the forces capabilities in each of the 7 dimension. The actuator torques  $\tau_{Fj}$  needed to produce a unitary force  $\hat{F}_j$ , where  $\hat{F}_j$  is a  $7 \times 1$  vector formed of null components except for the  $j^{th}$  which is 1, is given by  $\tau_{Fj} = (J^+) \hat{F}_j$ . All relations being linear, both the unitary force  $\hat{F}_j$  and corresponding actuator force vector  $\tau_{Fj}$  must be proportionally scaled such that the element in  $\tau_{Fj}$  with the highest absolute value is equal to the actuator torque limit  $\tau_{max}$ . Mathematically the force capability  $F_{max,j}$  in dimension  $j$  is given as:

$$F_{max,j} = \min_i \left| \frac{\tau_{max}}{\tau_{Fj,i}} \right| \tag{18}$$

where  $\tau_{Fj,i}$  is the  $i^{th}$  element of  $\tau_{Fj}$ . Hence, the calculation does not involve a numerical method and is much less computer-intensive than the sensitivity calculation presented in Section 5.2.

Motor torques are bounded by the stall torque specification of the selected motors (0.264 Nm) times the gearing transmission ratio (12) between the motors and the base joints, which will be described in Section 6. The stall torque specification can only be used for some period of time before the electric motors overheat. A more conservative evaluation can use the maximal continuous torque specification (0.0277 Nm) instead, which is valid for any rotational speed and any period of time. Stall torque can be used to present the operator a stiff interaction with a solid wall or object, which are normally not sustained for a period longer than a few minutes at a time, while the maximal continuous torque can be used other long-term continuous force feedback. Using the stall torque, the torque limit for the base joint is given by  $\tau_{i,max} = 0.264 \times 12 = 3.168$  Nm.

The maximal force for a certain configuration was calculated using Eq. (18). Some results are presented in Fig. 8 for the horizontal plane, with all other configuration parameters set to their central positions. Using the maximal continuous torque instead of the stall torque for the torque limit  $\tau_{i,max}$  will produce results approximately 10 times smaller. The force capabilities in the X and Y direction are very close to being symmetrical since the grasping value of 36 mm corresponds to a rhombus configuration that is close but not exactly the same as a square platform. Unlike the resolution graph presented in Fig. 7, the isolines for the force capabilities show sharp edges corresponding a transition from one motor to another being used to the maximal force.

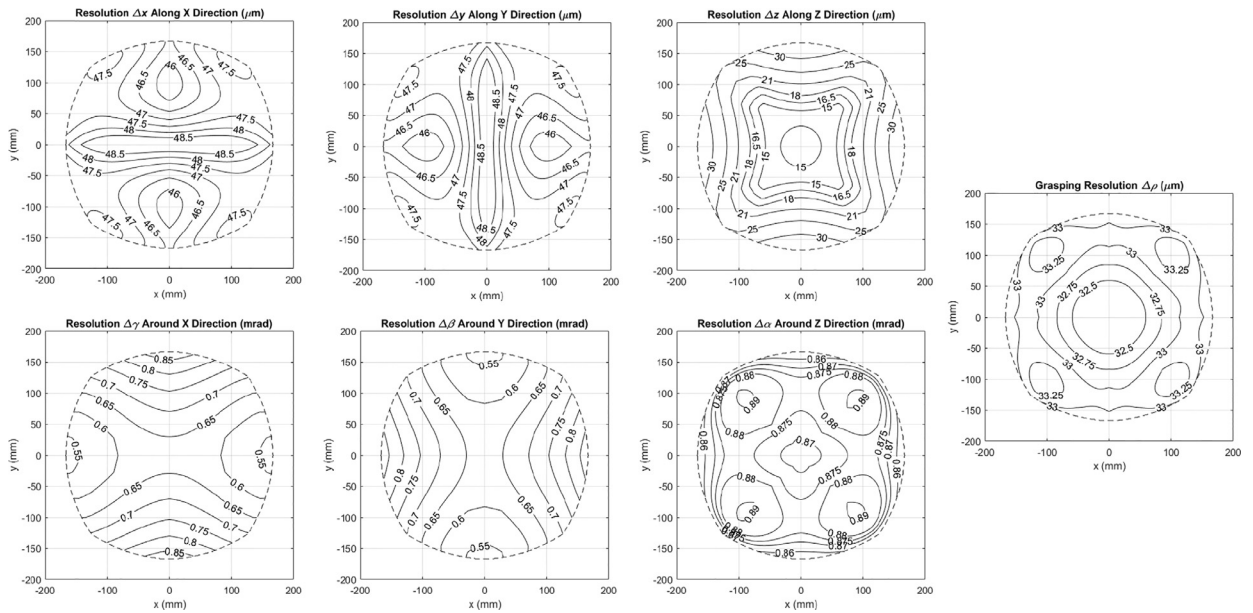


**Fig. 7.** Linear and angular resolution on the grasper tips when the platform is moving in the X–Y plane, while other configuration parameters are constant ( $z = 270$  mm,  $\alpha = 0$ ,  $\beta = 0$ ,  $\gamma = 0$ ,  $\rho = 36$  mm).

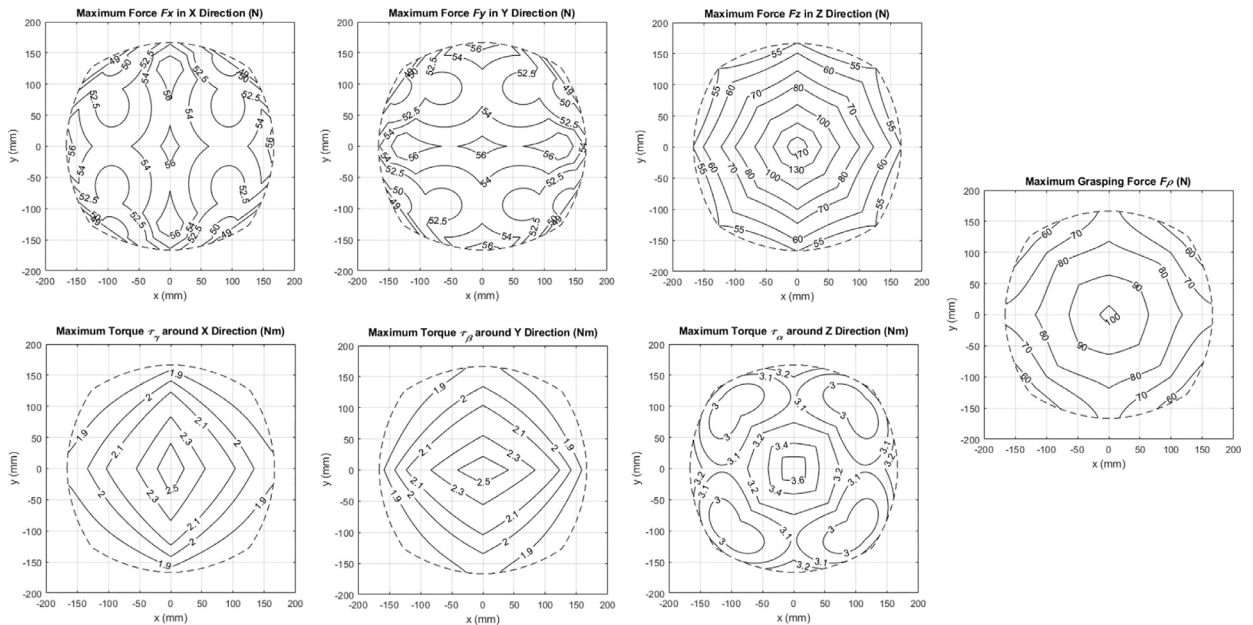


**Fig. 8.** Maximal forces and moments that can be applied on the fingertips when the platform is moving in the X–Y plane, while other configuration parameters are constant ( $z = 270$  mm,  $\alpha = 0$ ,  $\beta = 0$ ,  $\gamma = 0$ ,  $\rho = 36$  mm). The maximal torque on the base joints are limited to 3.168 Nm as defined by the stall torque of the actuators and by the transmission ratio.

In a compromise between high force capabilities and safety consideration, the selection of the actuators was made such that the maximal grasping force that can be transmitted is around 55 N, which corresponds to the maximal force an operator can usually exert with its fingers [23]. Comfortable forces should be at most 15% of the maximal forces, which is more in line with the mapping of the maximal continuous torques capabilities of the actuators to the fingertips.

Again, due to the fully parallel structure of the novel 7-DOF device, all performance indices are coupled in all 7 dimensions. In order to provide a complete overview of the force capabilities, a sampling of the maximal forces in each DOF over configurations in the 7 dimensions was performed and is presented in Table 4. The set of sampling points used is the same that was used in Table 3 of Section 5.2 for the same useful workspace corresponding to  $\pm 45^\circ$  angular ranges.

**Table 4**Force capabilities for each DOF over the full  $\pm 45^\circ$  useful workspace.

DOF	Center	Mean	SD	Best	Worst
$f_x$ (N)	56.8	42.4	0.02	70.5	28.5
$f_y$ (N)	56.9	42.6	0.01	70.3	25.9
$f_z$ (N)	218	67.2	0.04	229.3	7.9
$\tau_\alpha$ (Nm)	3.82	1.26	3e-4	4.01	0.22
$\tau_\beta$ (Nm)	2.68	1.93	5e-4	3.73	0.56
$\tau_\gamma$ (Nm)	2.68	1.58	5e-4	2.87	0.51
$f_\rho$ (Nm)	103.1	48.4	0.04	182.8	12.8

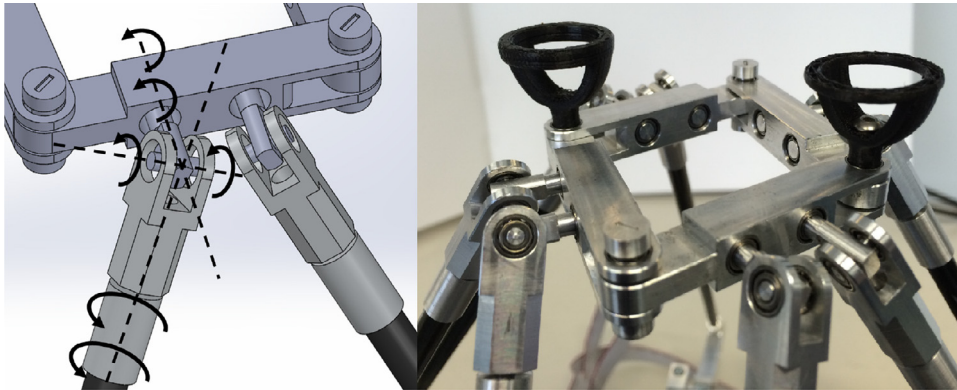


**Fig. 9.** Left: CAD model of the system of three coaxial revolute joints used to emulate a virtual spherical joint at the end of each leg. Each arrow corresponds to a ball bearing and the three axes of rotation are intersecting. Right: Implementation of the 8 spherical joints on the configurable platform.

It can be noted that the force capabilities in the horizontal plane ( $f_x$ ,  $f_y$ ,  $\tau_\alpha$ , and  $f_\rho$ ) are more homogeneous than the forces outside the plane. The average forces capabilities are quite above what is generally offered in commercial haptic devices, while the worst sampling point for the force in  $f_z$  is about the same as the maximal exertable force of common recent haptic devices, such as the 3D system Touch X.

## 6. Prototype implementation

This section describes the technical design and implementation of the 7-DOF parallel haptic device prototype. The technical design involves the selection of all other design parameters that do not influence the kinematics. These parameters were selected such that the prototype presents desirable technical properties for haptic applications such as low inertia, low friction, low backlash, high stiffness, and backdrivability.

### 6.1. Spherical joints

Eight spherical joints connect the parallel legs to the configurable platform. Ball-and-socket spherical joints are recognized for their limited angular workspace and high level of friction, which makes them not suitable for haptic devices. To avoid those drawbacks, the spherical joints are emulated by a series of three intersecting, perpendicular, revolute joints. This allows for a large angular workspace and greatly reduces the friction since the displacements are taken care of by a set of ball bearings instead of the sliding surfaces found in ball-and-socket joints. Kinematic design parameter 7, the offset between the platform and the spherical joints, presented in Section 4.1 was introduced to allow for this design. Each revolute joint is created by a set of two coaxial bearings, so 6 bearings are needed to emulate each spherical joint. Fig. 9 shows the drawing of one joint and the actual implementation of the 8 spherical joints i.e 48 bearings, on the configurable platform of the prototype. Despite the advantages of larger angular workspace and lower friction, one disadvantage of triple intersecting revolute joints compared to ball-and-socket joints is that the system possesses a serial singularity which occurs when the first axis of rotation and the third axis of rotation become perfectly aligned. In practice, this situation occurs only for some specific configurations far outside the useful workspaces defined in Section 5.

### 6.2. Link 2 and universal joint

A 2-DOF universal joint connects Link 1 and Link 2 of each leg, which allows yaw and pitch rotations between the two links. Universal joints are usually made of two intersecting revolute joints sharing a cross shaped pin as inner shafts.

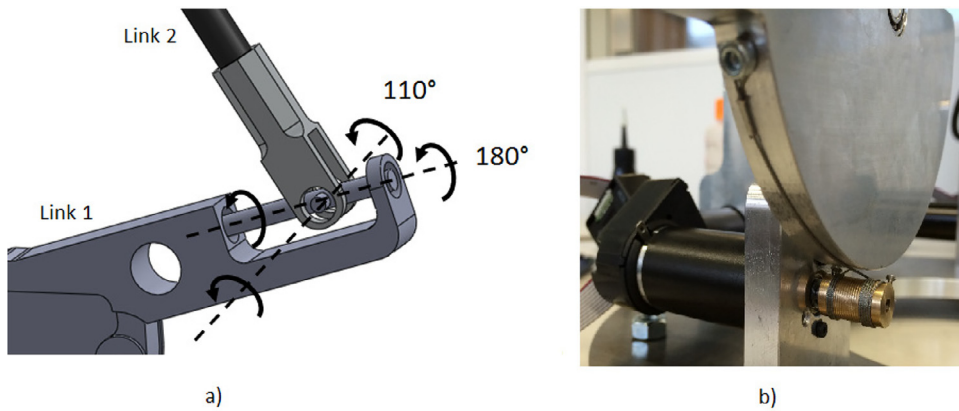


**Fig. 10.** a) Modified universal joint, with an elongated pin, allowing larger angular workspace. b) Capstan wired transmission used to reduce backlash.

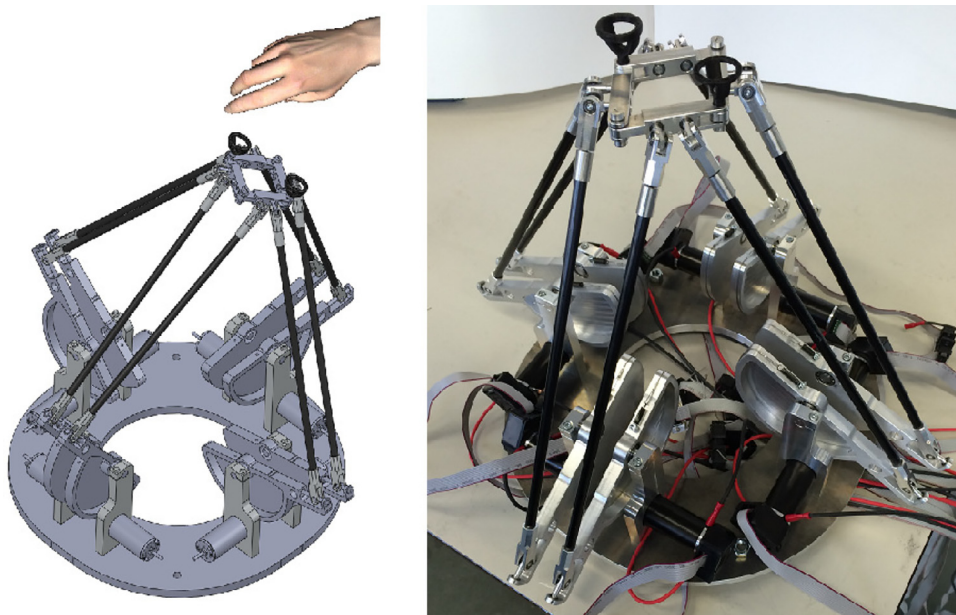


**Fig. 11.** CAD model and implementation of the 7-DOF parallel haptic device.

Commercially available universal joints are typically limited in their angular workspace and were not suitable for the range of angles needed. This was solved by elongating the first inner shaft in such a way that the second link can rotate  $180^\circ$  around it as shown on Fig. 10a. The two axes of rotation of the modified universal joints are able to reach  $180^\circ$  and  $110^\circ$  of angular workspace respectively. The second pin do not cross the first pin in its mid-distance but is slightly offset to minimize the risk of interference between the first and second link of the legs over the workspace.

### 6.3. Link 1 and capstan transmission

Conventional gearboxes generally introduce play and backlash, which decreases the performance of a haptic device. In order to realize high backdrivability, 8 capstan-wire transmissions were implemented in the prototype. The first link of each leg has a half circle surface which is connected with 2 cables to a grooved capstan glued on the motor shaft, as shown in Fig. 10b. The transmission ratio obtained is 12 and is defined by the ratio between the half circle radius and the capstan radius. Fig. 11 shows the CAD model of the technical design of the 7-DOF parallel as well as the actual prototype fully assembled.

### 6.4. Control hardware and software implementation

The device is actuated by eight Maxon DC-motors using graphite brushes and delivering 20 Watts each and providing, as mentioned in Section 5.3, a maximal continuous torque of 0.0277 Nm and a stall torque of 0.264 Nm. The rotation of

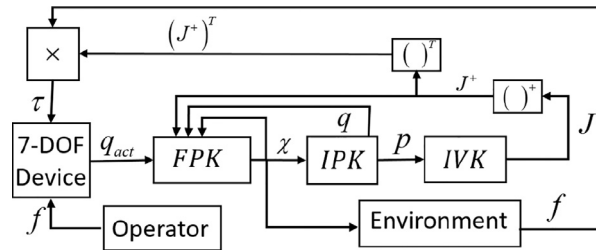


Fig. 12. Local software control for the master haptic device.

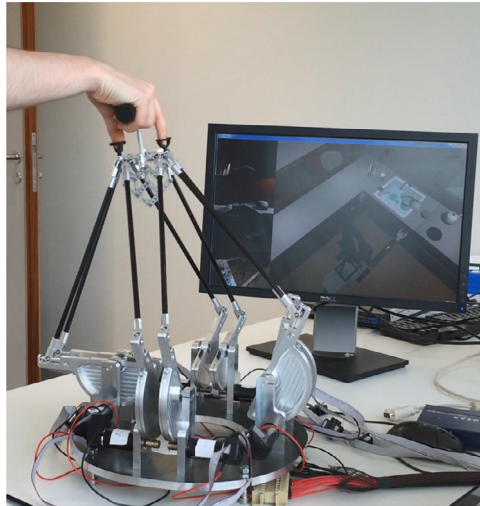


Fig. 13. The haptic device connected to a virtual slave and virtual environment. A special passive handle mechanism (not described in this article) is attached to the grasper tips to allow control from two fingers and the palm of the hand of the operator.

the motor shaft is measured with optical encoders, that can produce 1000 counts per turn. Using the quadrature of the encoder pulses, the resolution is multiplied by 4, which lead to a resolution of 1.57 mrad. Both the actuator torque and the encoder resolution are magnified by the capstan transmission with a factor of 12 and the effective specifications of the actuators/sensors are a stall torque of 3.168 Nm, a maximal continuous torque of 0.332 Nm, and a resolution of 0.131 mrad. These values define the sensing and actuation capabilities in the actuator space, which can be mapped into end-effector capabilities over the workspace using the kinematic procedures defined in Section 5.

The kinematics model of the device was implemented on a Bachmann MH200 series PLC hardware controller that can be programmed using Matlab/Simulink. Fig. 12 shows a schematic of the internal control for the master haptic side. FPK, IPK, and IVK stand for forward position, inverse position, and inverse velocity kinematics respectively. Inverse position kinematics is also used to produce the vector  $\mathbf{p}$ , a vector containing the positions and orientations of all the rigid links of the device. Those are needed to fill the elements of the Jacobian  $\mathbf{J}$ . Fig. 13 shows the haptic device using this controller to connect with a virtual environment.

## 7. Conclusion

This paper introduced a novel 7-DOF parallel haptic device, and its kinematic analysis, design, kinematic performance, and technical implementation were presented. The main innovation in this device is that it offers full position, orientation, and grasping capabilities while all the motors are located on the base. This is possible thanks to a special configurable platform, for which both the pose and configuration can receive force-feedback from 8 base-located motors, using only mechanical links and ball bearings. Analysis of the kinematic performance of the architecture, including its resolution and force-feedback mapping over the 7-DOF workspace, shows it can deliver acceptable haptic performance using conventional sensors and actuators.

## Supplementary material

Supplementary material associated with this article can be found, in the online version, at doi:[10.1016/j.mechmachtheory.2019.01.002](https://doi.org/10.1016/j.mechmachtheory.2019.01.002).



## References

- [1] M.H. Vu, U.J. Na, A new 6-dof haptic device for teleoperation of 6-dof serial robots, *Instrum. Meas. IEEE Trans.* 60 (11) (2011) 3510–3523.
- [2] J.M. Sabater, R.J. Saltarén, R. Aracil, Design, modelling and implementation of a 6-urs parallel haptic device, *Rob. Auton. Syst.* 47 (1) (2004) 1–10.
- [3] S.U. Lee, S. Kim, Analysis and optimal design of a new 6 dof parallel type haptic device, in: *Intelligent Robots and Systems, 2006 IEEE/RSJ International Conference on*, IEEE, 2006, pp. 460–465.
- [4] J.W. Yoon, J. Ryu, Y.-K. Hwang, Optimum design of 6-dof parallel manipulator with translational/rotational workspaces for haptic device application, *J. Mech. Sci. Technol.* 24 (5) (2010) 1151–1162.
- [5] L. Birglen, C. Gosselin, N. Pouliot, B. Monsarrat, T. Laliberté, Shade, a new 3-dof haptic device, *IEEE Trans. Rob. Autom.* 18 (2) (2002) 166–175.
- [6] L.-F. Lee, M.S. Narayanan, F. Mendel, V.N. Krovi, Kinematics analysis of in-parallel 5 dof haptic device, in: *Advanced Intelligent Mechatronics (AIM), 2010 IEEE/ASME International Conference on*, IEEE, 2010, pp. 237–241.
- [7] F. Gosselin, C. Bidard, J. Brisset, Design of a high fidelity haptic device for telesurgery, in: *Robotics and Automation, 2005. ICRA 2005. Proceedings of the 2005 IEEE International Conference on*, IEEE, 2005, pp. 205–210.
- [8] X. Kong, C.M. Gosselin, *Type synthesis of parallel mechanisms*, Springer Publishing Company, Incorporated, 2007.
- [9] J.-P. Merlet, *Parallel Robots*, 74, Springer Science & Business Media, 2012.
- [10] C. Gosselin, J. Angeles, Singularity analysis of closed-loop kinematic chains, *Rob. Autom. IEEE Trans.* 6 (3) (1990) 281–290.
- [11] Y. Tsumaki, H. Naruse, D.N. Nenchev, M. Uchiyama, Design of a compact 6-dof haptic interface, in: *Robotics and Automation, 1998. Proceedings. 1998 IEEE International Conference on*, 3, IEEE, 1998, pp. 2580–2585.
- [12] Z. Najdovski, S. Nahavandi, T. Fukuda, Design, development, and evaluation of a pinch-grasp haptic interface, *IEEE/ASME Trans. Mechatron.* 19 (1) (2014) 45–54.
- [13] M.G. Mohamed, C.M. Gosselin, Design and analysis of kinematically redundant parallel manipulators with configurable platforms, *Rob. IEEE Trans.* 21 (3) (2005) 277–287.
- [14] P. Lambert, *Parallel Robots with Configurable Platforms*, Delft University of Technology, TU Delft, 2013.
- [15] P. Lambert, J.L. Herder, Parallel robots with configurable platforms: fundamental aspects of a new class of robotic architectures, *Proc. Inst. Mech. En. Part C* (2015). 0954406215602511.
- [16] P. Lambert, J. Herder, A novel parallel haptic device with 7 degrees of freedom, in: *World Haptics Conference (WHC), 2015 IEEE, IEEE, 2015*, pp. 183–188.
- [17] B. Dasgupta, T. Mruthyunjaya, Force redundancy in parallel manipulators: theoretical and practical issues, *Mech. Mach. Theory* 33 (6) (1998) 727–742.
- [18] G. Liu, Y. Wu, X. Wu, Y. Kuen, Z. Li, Analysis and control of redundant parallel manipulators, in: *Robotics and Automation, 2001. Proceedings 2001 ICRA. IEEE International Conference on*, 4, IEEE, 2001, pp. 3748–3754.
- [19] J.A. Saglia, J.S. Dai, D.G. Caldwell, Geometry and kinematic analysis of a redundantly actuated parallel mechanism that eliminates singularities and improves dexterity, *J. Mech. Des.* 130 (12) (2008) 124501.
- [20] P. Cardou, S. Bouchard, C. Gosselin, Kinematic-sensitivity indices for dimensionally nonhomogeneous Jacobian matrices, *IEEE Trans. Rob.* 26 (1) (2010) 166–173.
- [21] H.Z. Tan, M.A. Srinivasan, B. Eberman, B. Cheng, Human factors for the design of force-reflecting haptic interfaces, *Dyn. Syst. Control* 55 (1) (1994) 353–359.
- [22] S.B. Nokleby, R. Fisher, R.P. Podhorodeski, F. Firmani, Force capabilities of redundantly-actuated parallel manipulators, *Mech. Mach. Theory* 40 (5) (2005) 578–599.
- [23] K.B. Shimoga, A survey of perceptual feedback issues in dexterous telemanipulation. II. finger touch feedback, in: *Virtual Reality Annual International Symposium, 1993.*, 1993 IEEE, IEEE, 1993, pp. 271–279.